J. Mech. Phys. Solids 210 (2026) 106530

Contents lists available at ScienceDirect

Journal of the Mechanics and Physics of Solids

journal homepage: www.elsevier.com/locate/jmps

Coupled grain-pore fabric evolutions in sheared granular materials: Anisotropy lagging and geometric emergence

Amiya Prakash Das [a,*], Jidong Zhao [a,*], Thomas Sweijen [b]

[a] Department of Civil and Environmental Engineering, Hong Kong University of Science and Technology, Clearwater Bay, Kowloon, Hong Kong SAR
[b] Department of Earth Sciences, Faculty of Geosciences, Utrecht University, Utrecht, the Netherlands

ARTICLE INFO

Keywords:
Fabric anisotropy
Minkowski functionals
Pore-scale metrics
Polydispersity
DEM

ABSTRACT

The morphological evolution of pore spaces is a critical yet poorly quantified microstructural determinant of the macroscopic mechanical and hydraulic behavior of granular materials. While the anisotropy of the grain contact network (F_c) is known to dictate material response, the concurrent evolution of pore space anisotropy (F_p) and its coupling with F_c remains inadequately understood. This study employs Minkowski moment tensor analysis within a Discrete Element Method (DEM) framework to bridge this gap. We systematically investigate dense and loose, monodisperse and polydisperse assemblies under cyclic triaxial loading to quantify the dynamic coupling between F_c and F_p. We demonstrate a moderate to strong correlation between F_c and F_p, with a systematic lag in the response of F_p attributed to hierarchical geometric emergence across scales. This lag is constrained by particle-scale free-volume reorganization and its kinematic compatibility with particle motion. Additionally, key pore-scale metrics, including inverse Voronoi cell fractions (ϕ_v^{-1}), pore-scale porosity (ϕ_p), and pore shape anisotropy $\hat{\beta}$, are well described by gamma distributions across all packing densities and strain levels. Notably, the scaled ϕ_v^{-1} follows a k-gamma distribution, providing a statistically consistent descriptor for volume fluctuations. A strong correlation is also observed between the average pore shape factor ($|\beta|_{avg}$) and global porosity, suggesting that $|\beta|_{avg}$ serves as a geometry-based descriptor linking collective pore deformation to packing density. These findings underscore the utility of the Minkowski tensor approach in capturing 3D fabric evolution and explicitly linking pore- and grain-scale interactions. The quantitative relationships and statistical descriptors presented here provide a new foundation for enhancing constitutive models in geotechnics and powder technology, offering insights relevant to future investigations into permeability evolution and shear band formation.

1. Introduction

Granular materials derive their macroscopic mechanical and transport properties from microstructural characteristics which are collectively termed *fabric* encompassing the spatial arrangement, orientation, and interactions of particles, as well as the geometry and connectivity of void spaces. Fabric tensors provide a mathematical basis for quantifying these directional features, capturing the anisotropic distribution of particles, contacts, and pores within granular assemblies (Li and Li, 2009; Guo and Zhao, 2013; Sufian et al., 2019b). This microstructural representation is crucial for predicting key engineering behavior, including small-strain stiffness (Kuwano and Jardine, 2002; Wang and Mok, 2008), peak strength (Arthur and Menzies, 1972; Ventouras and Coop, 2009;

---

* Corresponding authors.
E-mail addresses: apdas@connect.ust.hk (A.P. Das), jzhao@ust.hk (J. Zhao), t.sweijen@uu.nl (T. Sweijen).

https://doi.org/10.1016/j.jmps.2026.106530
Received 4 October 2025; Received in revised form 14 January 2026; Accepted 25 January 2026

Li and Li, 2009), shear dilatancy (Cresswell and Powrie, 2004; Wan and Guo, 2004), and fluid permeability (Chan and Kenney, 1973; Kuhn et al., 2015). Moreover, the topological organization of pore networks, particularly their connectivity and the presence of closed particle chains (loop structures), plays a fundamental role in controlling fluid flow, energy dissipation, and strain localization (Vlahinić et al., 2014; Chueire et al., 2023; Ma et al., 2024). The analysis of these topological descriptors via network-based frameworks necessitates a unified view of the solid and void phases (Russell et al., 2016; Deng et al., 2021; Mei et al., 2023; Jiang et al., 2025). Comprehensive characterization of fabric tensors defined for these phases is therefore vital for predicting and optimizing macroscopic mechanical and transport properties across disciplines such as geomechanics and materials science.

Among various fabric descriptors, the contact-normal-based fabric tensor has been extensively studied using Discrete Element Method (DEM) due to its direct connection to force transmission mechanisms (Oda, 1982; Rothenburg and Bathurst, 1989; Ouadfel and Rothenburg, 2001; Guo and Zhao, 2013). Complementary tensors based on contact forces and particle orientations further enrich this framework, enabling detailed tracking of anisotropy evolution under loading, which is essential for advanced constitutive modeling (Li and Dafalias, 2012; Gao et al., 2014). However, while contact-based tensors dominate the literature, void-based fabric tensors remain comparatively underexplored despite their significant influence on both mechanical response and hydrogeological behavior (Sufian et al., 2015, 2019b).

Quantifying fabric tensors requires high-resolution data on particle geometries, spatial positions, inter-particle contact normals, and force transmission that are notoriously difficult to capture comprehensively in experiments. Traditional laboratory techniques, such as photoelasticity, have provided invaluable, direct visualization of grain-scale force chains and fabric evolution (Oda et al., 1985; Majmudar and Behringer, 2005). However, these methods are predominantly confined to two-dimensional (2D) systems employing disk-shaped particles. While high-resolution X-ray computed tomography (CT) has emerged as a powerful tool for 3D imaging and non-destructive characterization of particle morphologies and contact points (Desrues, 2004; Fonseca et al., 2012; Kawamoto et al., 2018), it still struggles to resolve dynamic contact forces during loading. This limitation hinders a comprehensive, force-informed understanding of fabric evolution (Li and Juanes, 2024). In this context, the DEM provides a powerful computational alternative, offering complete access to particle-scale kinematics and contact forces with high fidelity. We therefore leverage DEM in this study to investigate the evolution of internal fabric, with a specific focus on under-explored, void-based descriptors that complement established contact-based metrics.

The void structure is an integral component of granular fabric, yet its quantitative description poses unique challenges. Early methodologies, such as the scanning line technique pioneered by Oda et al. (1985), sought to characterize void orientation, leading to the definition of a 3D void fabric tensor (Inglis and Pietruszczak, 2003). This approach was later refined for 2D digital images by Ghedia and O'Sullivan (2012) to capture average void directionality and length within shear bands. Alternative frameworks have also been proposed: a graph-theoretical approach represents voids as loops enclosed by branch vectors (Satake, 1992; Kuhn, 1999), while a tessellation-based method defines void cell systems via modified Delaunay-Voronoi partitions at contact points (Li and Li, 2009). Building on the latter, Fu and Dafalias (2015) incorporated both directional distribution and void vector lengths, revealing a strong correlation between void- and contact normal-based fabric tensors in 2D DEM simulations of non-elongated particles. This is a finding that powerfully underscores the interconnectedness of solid and void phase evolution. Parallels can be drawn to cellular solids and foams, where macroscopic mechanical responses are intimately tied to the morphological and topological features of internal voids (Saadatfar et al., 2012; Blatny et al., 2023), such as how initial pore alignment influences anisotropic deformation and shear band formation.

Despite these advances, existing void-based fabric tensors often rely on simplified geometric proxies (e.g., mean lengths and elongation ratios) that fail to fully capture the complex 3D topology and shape anisotropy of pore spaces. This critical limitation motivates the present study, in which we introduce Minkowski tensors, a rigorous mathematical framework from integral geometry, to characterize void fabric (Schröder-Turk et al., 2011, 2013). Unlike traditional second-order tensors, Minkowski tensors provide a hierarchy of shape descriptors (e.g., volume, surface area, curvature) that encode both magnitude and directional properties, offering a richer and more comprehensive representation of anisotropy. By integrating Minkowski tensors into DEM simulations, we bridge the gap between contact- and void-based fabric descriptions, extending insights from Fu and Dafalias (2015) into 3D. This approach not only deepens our understanding of fabric evolution under loading but also lays the foundation for constitutive models that explicitly account for the coupled mechanical roles of the solid and void phases.

Our investigation is framed within the context of critical state soil mechanics, where granular fabric evolves toward a steady state under sustained shear. Understanding how void fabric aligns with the critical state offers new pathways to unravel fabric-stiffness coupling and refine constitutive laws with path-independent descriptors. The remainder of this paper is structured as follows: Section 2 details the DEM framework and the methodology for computing contact- and void-based fabric tensors, including the Minkowski tensor formalism. Section 3 describes the DEM model setup, and Section 4 analyzes fabric evolution under cyclical triaxial compression, explores the interrelation between different fabric descriptors. Finally, Section 5 summarizes the key findings and outlines future research directions for integrating topological void measures into multiscale constitutive frameworks.

2. Methodology

This section outlines the methodological framework employed in this study. The analysis begins with pore unit extraction, where we delineate the pore network within granular assemblies using regular triangulation and a subsequent merging algorithm. Subsequently, we compute the contact-based fabric tensor to quantify anisotropy in the spatial distribution of inter-particle contacts. To characterize the void phase, we then apply Minkowski tensors to measure pore shape anisotropy. Finally, we derive a pore orientational tensor to determine the principal directions of pore units, thereby extending our analysis to their directional anisotropy and enabling a direct

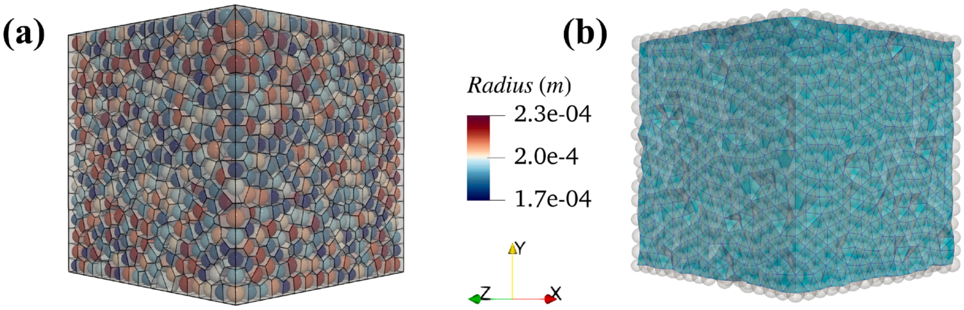

Fig. 1. (a) Voronoi tessellation of a polydisperse granular assembly, illustrating the partitioning of space based on particle neighborhood. The color gradient indicates varying particle radii, with values ranging from 1.7×10^{-4} m to 2.3×10^{-4} m. (b) Regular triangulation of the same assembly, highlighting the connectivity between particles and pores.

comparison with the contact fabric. Unless otherwise specified, this study considers assemblies comprising only spherical particles. This approach eliminates the need for other factors that contribute to fabric anisotropy, like branch vectors related to non-spherical particles. These vectors can introduce additional shape-induced anisotropies in contact networks (Satake, 1992; Kuhn, 1999). By simplifying the analysis, we focus more on the evolutions observed at the pore and contact scales.

2.1. Pore unit extraction

The pore space within a granular system exhibits geometric heterogeneity, consisting of relatively open void regions interconnected by narrow constrictions, typically located near particle-particle contacts, where the solid surface-to-pore volume ratio is relatively large. These constrictions play a dominant role in controlling transport, capillarity, and local mechanical interactions (Das et al., 2025). The pore space is subdivided into pore units, representing pore bodies, which are connected by pore throats that mediate connectivity between them (Catalano et al., 2014; Yuan and Chareyre, 2017). Although the void phase is topologically continuous and formally constitutes a single connected domain, it contains locally expanded cavities separated by narrow pore throats. The subdivision into pore units, therefore, reflects a coarse-grained model based on the geometric contrast between pore bodies and pore throats.

Pore unit extraction in this study proceeds through a two-stage process to delineate the pore-scale network within the granular system. An initial geometric discretization of the pore space is obtained using regular triangulation (weighted Delaunay) mapped from particle positions and radii (Catalano et al., 2014). Fig. 1 illustrates the geometric duality between the Voronoi tessellation and the regular triangulation adopted for pore unit construction, highlighting the spatial partitioning and pore connectivity of the granular assembly. The regular triangulation partitions the void space into grain-based tetrahedra T_i, each enclosing a localized pore volume bounded by four neighboring particles, see Fig. 2a. At this stage, the discretization over-segments the pore space: individual tetrahedra serve as elementary geometric units and do not yet correspond to physical pores. The facet of the adjoining tetrahedron encompasses the pore throat separating adjacent void regions. Each grain-based tetrahedron T_i is associated with a pore volume V_i, from which an effective pore radius is defined as

$$r_i = \chi V_i^{1/3}, \tag{1}$$

where χ is a dimensionless shape factor that maps the void volume to an equivalent regular shape of identical volume (Sweijen et al., 2018). The use of equivalent regular pore shapes follows the framework established in Joekar-Niasar et al. (2010) and Sweijen et al. (2018), providing a scalar measure of pore size suitable for geometric comparison during pore assembly.

To identify physically meaningful pore bodies, the grain-based tetrahedra are assembled into pore units through an iterative throat-controlled merging algorithm. For each pair of neighboring tetrahedra T_i and T_j, the void opening connecting them is characterized by a pore throat radius r_{ij}. Two neighboring tetrahedra are merged when the ratio of the connecting throat radius to the pore body size exceeds a threshold, i.e., $r_{ij}/r_i \geq \varphi$, where φ is a dimensionless merging criterion. This condition identifies pore throats that do not act as effective narrow geometric constrictions. The merging procedure is hierarchical and iterative in nature, see Fig. 2. The criterion φ is progressively reduced from an initially large value toward a prescribed lower bound $\varphi_{\min} = 0.90$, such that tetrahedra connected through wide openings are merged first, followed by those connected through progressively smaller openings as the criterion is relaxed (Sweijen et al., 2018). After each merging event, the pore unit volume is updated as the sum of the constituent tetrahedral void volumes, and a new effective pore radius is recomputed using the same volume-radius relation, Eq. (1). All neighboring throat-to-body ratios are then re-evaluated using the updated pore size, allowing pore units to emerge dynamically from the evolving local geometry rather than from a single-pass classification. Fig. 3 shows the particle configuration associated with an individual tetrahedron and a merged pore unit (coordination number 16), along with their corresponding Voronoi cells.

The number of tetrahedra that may be merged into a single pore unit is capped at a coordination number of 20, which prevents unphysical chaining through elongated void regions, (Sweijen et al., 2018). This constraint acts as numerical regularization, does not affect pore connectivity or total pore volume, but rather stabilizes higher-order pore-scale statistics. The robustness of the pore unit definition is assessed by examining pore-scale statistical distributions across representative volume elements with increasing

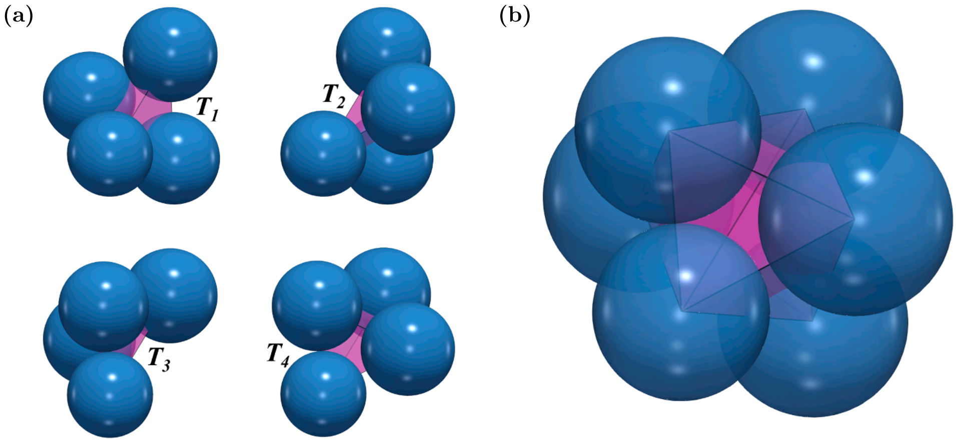

Fig. 2. Schematic illustration of pore unit extraction using an iterative throat-controlled merging algorithm. (a) Regular triangulation over-segments the continuous void space into grain-based tetrahedra T_i, each enclosing a localized void volume bounded by surrounding particles. (b) Neighboring tetrahedra, for instance T_1 and T_2, are merged when the pore throat connecting them has a radius r_{12} larger than the pore body radius r_1, i.e., $r_{12}/r_1 > \varphi$. The merged pore unit has a volume equal to the sum of the constituent void volumes, from which a new effective pore radius is computed.

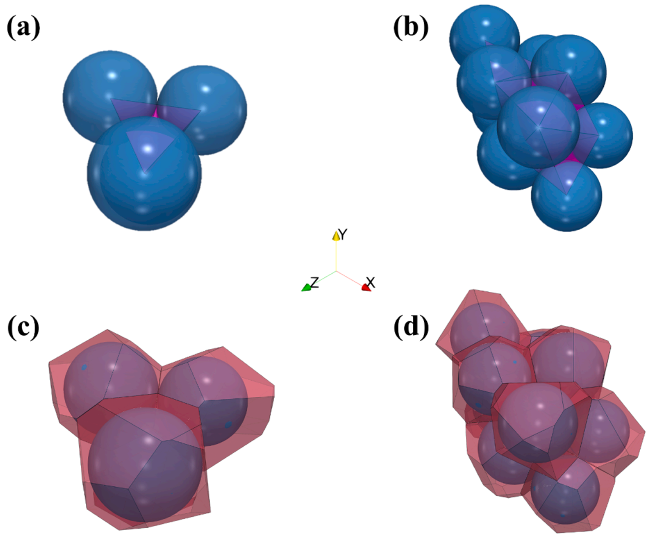

Fig. 3. (a) Pore unit with a coordination number of 4, illustrating the arrangement of particles. (b) Merged pore unit with a coordination number of 16, demonstrating a more complex connectivity. (c) Voronoi cells for the 4-particle system, highlighting the spatial partitioning of the neighboring region. (d) Voronoi cells for the 10-particle system.

particle numbers, as shown in Fig. 4. The convergence and statistical stability of normalized pore radii, throat radii, and pore-scale porosity distributions demonstrate that the resulting pore-scale descriptors are primarily sensitive to local geometric contrast and are not sensitive to system size or to the specific realization of the iterative merging process.

2.2. *Contact fabric anisotropy*

The contact-based fabric tensor quantifies the averaged spatial distribution of inter-particle contact orientations within a representative volume element (RVE) of a granular assembly. This tensor provides a fundamental measure of anisotropy in the contact network, reflecting how contact normals (unit vectors aligning with the direction of contact forces) organize under loading or structural constraints. Following the definition proposed by Oda (1982), the contact fabric tensor is expressed as:

$$\phi_{ij} = \frac{1}{N_c}\sum_{k=1}^{N_c} n_i^k n_j^k = \oint_{\Omega} E(\Omega) n_i n_j \, d\Omega, \tag{2}$$

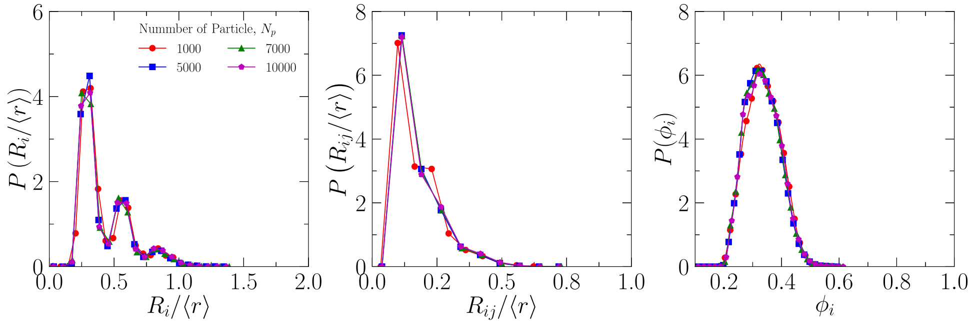

Fig. 4. Pore-scale statistical distributions for representative volume element with varying numbers of particles. (Left) Normalized pore radii ($R_i/\langle r\rangle$), (Middle) Normalized throat radii ($R_{ij}/\langle r\rangle$) and (Right) Pore porosity (ϕ_i).

where N_c denotes the total number of inter-particle contacts, n_i^k represents the i-th component of the unit normal vector for the k-th contact, and $E(\Omega)$ is the angular distribution density of these vectors over the unit sphere Ω. The summation form captures the discrete contributions of individual contacts, while the integral form reflects the continuous distribution, linking microscopic contact orientations to macroscopic fabric properties.

The distribution density $E(\Omega)$ describes the likelihood of contact normals aligning in specific directions, assumed here to be symmetric about the origin (Ken-Ichi, 1984; Sitharam et al., 2009). It is formulated as:

$$E(\Omega) = \frac{1}{4\pi}\left(1 + a_{ij}n_i n_j\right), \tag{3}$$

where a_{ij} is a second-order anisotropy tensor that quantifies deviations from isotropy. The factor $1/4\pi$ ensures normalization over the unit sphere for an isotropic case, while the term $a_{ij}n_i n_j$ introduces directional bias. This tensor a_{ij} is derived from the deviatoric part of ϕ_{ij}, defined as:

$$a_{ij} = \frac{15}{2}\phi'_{ij} \quad \text{where} \quad \phi'_{ij} = \phi_{ij} - \frac{\phi_{ii}}{3}\delta_{ij}, \tag{4}$$

with ϕ'_{ij} representing the traceless deviatoric component of the fabric tensor, and δ_{ij} the Kronecker delta. The coefficient $15/2$ scales a_{ij} to align with probabilistic interpretations of anisotropy, as established in prior work (Ken-Ichi, 1984).

To measure the degree of contact fabric anisotropy, we compute the scalar invariant F_c, given by:

$$F_c = \sqrt{\frac{3}{2}a_{ij}a_{ij}}, \tag{5}$$

where the repeated indices imply summation. This invariant, rooted in the second moment of a_{ij}, quantifies the magnitude of anisotropy in the contact network, with $F_c = 0$ indicating an isotropic distribution and increasing values reflecting stronger directional preference. Together, these expressions provide a robust framework for analyzing how contact fabric evolves, offering insights into the microstructural basis of macroscopic mechanical behavior in granular materials.

2.3. Minkowski tensors for shape anisotropy

Minkowski tensors provide a robust framework for quantifying the shape anisotropy of a 3D body K, encompassing both convex and non-convex geometries. These tensors yield six independent, symmetric rank-2 metrics —denoted $W_0^{2,0}$, $W_1^{2,0}$, $W_2^{2,0}$, $W_3^{2,0}$, $W_1^{0,2}$, and $W_2^{0,2}$ —whose eigenvalues map to an ellipsoid in Euclidean space. The degree of anisotropy is derived from the ratio of the minimum to maximum eigenvalues, offering a scalar measure of directional bias (Schröder-Turk et al., 2011). For a body K with bounding surface ∂K, these tensors are defined as:

$$W_0^{2,0} = \int_K r \otimes r \, dV, \tag{6}$$

$$W_1^{2,0} = \frac{1}{3}\int_{\partial K} r \otimes r \, dA, \tag{7}$$

$$W_2^{2,0} = \frac{1}{3}\int_{\partial K} H(r)\, r \otimes r \, dA, \tag{8}$$

$$W_3^{2,0} = \frac{1}{3}\int_{\partial K} G(r)\, r \otimes r \, dA, \tag{9}$$

$$W_1^{0,2} = \frac{1}{3}\int_{\partial K} n \otimes n \, dA, \tag{10}$$

$$W_2^{0,2} = \frac{1}{3}\int_{\partial K} H(r)\, n \otimes n \, dA, \tag{11}$$

where r is the position vector from a chosen origin, n is the outward unit normal to ∂K, and the dyadic product $r \otimes r = r_i r_j$ (or $n \otimes n = n_i n_j$) forms a symmetric tensor. The terms $H(r)$ and $G(r)$ denote the mean and Gaussian curvatures at point r on the surface, respectively. The factor $1/3$ ensures normalization consistent with geometric conventions (Schröder-Turk et al., 2011).

These six tensors capture distinct morphological features of K. The first four —$W_0^{2,0}$, $W_1^{2,0}$, $W_2^{2,0}$, and $W_3^{2,0}$ —are moment tensors, analogous to moments of inertia. For a body with unit density, the inertia tensor I is:

$$I = \int_K (\|r\|^2 E_3 - r \otimes r)\, dV, \tag{12}$$

where E_3 is the 3D identity matrix. The relationship between $W_0^{2,0}$ and I is:

$$W_0^{2,0} - \mathrm{tr}(W_0^{2,0}) E_3 = I, \tag{13}$$

with $\mathrm{tr}(W_0^{2,0})$ as the trace. Thus, $W_0^{2,0}$ quantifies the volumetric mass distribution about a reference point, typically the centroid. The additive property of Minkowski tensors, rooted in their convex-body origins, extends their applicability to non-convex shapes (Schröder-Turk et al., 2011).

In this study, we employ $W_0^{2,0}$ to compute the anisotropy of pore units (cells) within granular assemblies (Xing et al., 2024). This moment tensor, which reflects the volumetric shape, is calculated using a Python-based algorithm adapted from the open-source Karambola code (Schröder-Turk et al., 2011). The computation proceeds as follows:

1. Triangulate the surface facets of the pore unit.
2. Construct tetrahedra by connecting each facet to the centroid as the reference point.
3. Compute the moment contribution of each tetrahedron and sum these to obtain $W_0^{2,0}$.

This process subdivides the volume into tetrahedra anchored at the centroid for a polyhedron with convex facets, which serves as the reference point for computing position vectors r in Eq. (6). The total $W_0^{2,0}$ is the sum of individual tetrahedral contributions, leveraging the tensors' additivity to ensure consistency across the pore's geometry.

The Minkowski tensor is utilized effectively to quantify the anisotropies and the shapes of the spatial bodies (Schröder-Turk et al., 2010, 2011). For a given body K, the maximum, intermediate, and minimum eigenvalues of the second-order Minkowski moment tensor, $\lambda_{\max} \geq \lambda_{\mathrm{int}} \geq \lambda_{\min}$, encode the principal geometric directions and their relative extents. Although ratios of extremal eigenvalues have been widely used to quantify the degree of anisotropy, such measures do not explicitly incorporate the role of the intermediate eigenvalue and are often unable to distinguish between different classes of anisotropic shapes, like prolate or oblate.

In this work, the pore shape anisotropy is quantified using a scalar measure that explicitly includes all three eigenvalues of the Minkowski tensor:

$$\beta = \frac{\lambda_{\max} + \lambda_{\min} - 2\lambda_{\mathrm{int}}}{\lambda_{\mathrm{mean}}}, \tag{14}$$

where the mean eigenvalue is defined $\lambda_{\mathrm{mean}} = (\lambda_{\max} + \lambda_{\min} + \lambda_{\mathrm{int}})/3$. The numerator of β represents the ordering of the eigenvalues and characterizes the relative position of the intermediate eigenvalue within the eigen space. As a result, β explicitly encodes pore shape anisotropy: $\beta < 0$ corresponds to prolate-dominated geometries and $\beta > 0$ indicate oblate-dominated geometries. Isotropic pore geometries are characterized by $\beta = 0$ (Guo and Zhao, 2014).

For a given granular assembly, an ensemble-averaged pore shape factor is defined as

$$|\beta|_{avg} = \frac{1}{N_p}\sum_{i=1}^{N_p} |\beta_i|, \tag{15}$$

where β_i denotes the pore shape anisotropy parameter of the i-th pore and N_p is the total number of identified pores. The absolute value is adopted to quantify the magnitude of pore shape anisotropy independent of orientation, consistent with the scalar nature of the macroscopic correlations.

2.4. Pore orientational tensor and anisotropy

The application of the Minkowski moment tensor extends beyond quantifying the shape anisotropy of a body K. The moment tensor is also employed to calculate the principal orientation of an individual pore unit. This principal orientation is determined through eigen decomposition, where the eigenvalues (λ) and eigenvectors (p) define the shape anisotropy and principal orientation of the pore unit, respectively. The major, intermediate, and minor orientation axes correspond to the maximum, intermediate, and minimum

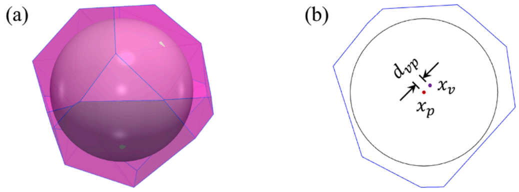

Fig. 5. (a) Three-dimensional Voronoi cell associated with a particle, illustrating the local pore geometry used for Minkowski tensor analysis. (b) Two-dimensional schematic showing the distance d_{vp} between the Voronoi cell centroid, x_v and the particle center, x_p.

eigenvalues, respectively (Sufian et al., 2015). Following the definition of a "local void vector" in Konishi and Naruse (1988), the principal eigenvector of a pore unit can be used to compute the pore orientation tensor ($\mathbb{P}_{ij}$), Eq. (16).

$$\mathbb{P}_{ij} = \frac{1}{N_p} \sum_{k=1}^{N_p} p_i^k p_j^k = \oint_{\Omega} E(\Omega) p_i p_j \, d\Omega, \tag{16}$$

where N_p is the total number of pore units in the granular assembly and p_i^k represents the i-th component of the principal eigenvector of the k-th pore unit. Similar to the angular distribution function of the contact normal vectors, a symmetric distribution density $E(\Omega)$ can also be expressed for the directional distribution of the pore orientation tensor, Eq. (17) (Ken-Ichi, 1984).

$$E(\Omega) = \frac{1}{4\pi}(1 + \mathbb{P}_{ij} p_i p_j), \tag{17}$$

where $\mathbb{P}_{ij}$ is the second order anisotropy pore fabric tensor defined as

$$p_{ij} = \frac{15}{2} \mathbb{P}_{ij}', \quad \text{where } \mathbb{P}_{ij}' = \mathbb{P}_{ij} - \frac{\mathbb{P}_{ii}}{3}. \tag{18}$$

The following invariant of p_{ij} is used to quantify the degree of anisotropy (F_p) of the pore-based fabric tensor,

$$F_p = \sqrt{\frac{3}{2} p_{ij} p_{ij}}. \tag{19}$$

2.5. Voronoi-based particle cell geometry and kinematic descriptor

The local geometry of the void space surrounding individual particles is characterized using Voronoi tessellation. For each particle, the associated Voronoi cell defines the region of space closer to that particle than to any other, providing a particle-centered partition of the pore space, see Fig. 3 and Fig. 5a. Whereas pore units represent coarse-grained cavities formed by multiple grains, Voronoi cells capture the pore geometry at the particle scale and are therefore suited for quantifying local pore shape and pore-particle kinematics. The anisotropy of each Voronoi cell is quantified using the second-order Minkowski tensor $W_0^{0,2}$. The same tensorial formalism is applied to Voronoi cells as described in Section 2.3, enabling a consistent comparison between particle-centered and pore-centered geometric descriptors, F_v and F_p, respectively. F_v is quantified as

$$F_v = \sqrt{\frac{3}{2} v_{ij} v_{ij}}, \tag{20}$$

where v_{ij} is 15/2 times the deviatoric part of $\mathbb{V}_{ij}$ tensor, similar to one defined in Eq. (16), averaged over the number of Voronoi cells (or number of particles).

A kinematic descriptor is introduced to quantify the relative positioning of the pore space with respect to the particle. This descriptor d_{vp} is defined as the Euclidean distance between the centroid of the Voronoi cell and the center of the corresponding particle

$$d_{vp} = \left\| x_v - x_p \right\|, \tag{21}$$

where x_v is the centroid of the Voronoi cell and x_p is the particle center. The quantity d_{vp} provides a scalar measure of the geometric offset between the particle and its surrounding pore space, see Fig. 5b.

3. Details of simulations

3.1. Discrete element method

The open-source code Yade-DEM is used to perform simulations (Šmilauer et al., 2010). In this study, spherical particles are modeled using a soft-sphere contact approach, where the Hertz-Mindlin theory of elastic deformation governs interactions between particles. Yade-DEM incorporates the "Computational Geometry Algorithms Library" (CGAL), which ensures precise calculations of predicates and highly efficient triangulation algorithms, crucial for establishing accurate pore-scale networks within the packing.

Table 1
Properties of monodisperse and polydisperse granular packings for loose and dense configurations.

Property	Monodisperse		Polydisperse	
	Loose (ML)	Dense (MD)	Loose (PL)	Dense (PD)
Particle radius, r (mm)	0.2	0.2	$0.2 \pm 0.2r$	$0.2 \pm 0.2r$
Porosity	0.388	0.437	0.381	0.435

The Hertz-Mindlin contact model is used to compute the elastic forces, where it is assumed that small deformations occurred at contact points between two particles, resulting in δ_{ij}^n being much smaller than $\min(r_i, r_j)$. The normal component of the contact force, denoted F_{ij}^n is given according to Johnson and Johnson (1987) and Thornton et al. (2011)

$$F_{ij}^n = -k_{ij}^n \left(\delta_{ij}^n\right)^{3/2}. \tag{22}$$

where k_{ij}^n is the contact stiffness in the normal direction. At each time step, the tangential component F_{ij}^s is computed as a function of shear increment Δu_s Eq. (23). Sliding may occur at contact if the tangential force exceeds a threshold value set by the coefficient of friction

$$\left(F_{ij}^s\right)^t = \left(F_{ij}^s\right)^{t-\Delta t} + k_{ij}^s \Delta u_s t. \tag{23}$$

The contact force between two particles is represented by F_{ij}^c, which is the sum of the normal and tangential forces denoted by F_{ij}^n and F_{ij}^s, respectively. The particle acceleration is computed using Newton's second law to solve the coupled system, incorporating contact, gravitational, and fluid forces. The velocity and position of each particle are obtained by integrating the acceleration vector. Tangential forces F_{ij}^s are incrementally calculated using the tangential displacement, and sliding occurs when the tangential force exceeds the Coulomb friction limit, $F_{ij}^s \le \mu F_{ij}^n$.

3.2. Model setup

To explore the effects of particle size distribution on fabric evolution, two RVEs are generated: one with a monodisperse particle distribution and another with a polydisperse distribution. In the polydisperse granular assembly, particles have an average radius of 0.2 mm with a specified size variation, while the monodisperse assemblies employ uniform-size particles. Dense and loose packing states are achieved by manipulating inter-particle friction angles during isotropic compression.

Creating a dense RVE begins with an initial setup of spherical particles randomly distributed within a cubic domain of $0.02 \times 0.02 \times 0.02$ m^3. The inter-particle friction angle is initially lowered to 1°, resulting in an initial porosity exceeding 0.90 due to the sparse and disordered arrangement of the particles. Servo-controlled walls are then gradually moved to densify the packing until a statically homogeneous state is achieved under an isotropic confining stress of 100 kPa. Once this state is reached, the friction angle is restored to 30°, a typical value for realistic granular materials such as silica sand, which stabilizes the assembly. This process yields a final porosity of approximately 0.38 for the dense packing, while the loose packing maintains a higher porosity. Table 1 lists the details for simulation and initial porosities of the RVEs.

To determine the RVE size, we analyzed the effect of particle number on the mechanical response using datasets with 1000, 5000, 7000, and 10,000 particles. Fig. 6a presents the stress ratio (q/p) vs. axial strain (ϵ_a) alongside the average stress ratio. We evaluated the variation in q/p at specific ϵ_a levels of 1, 5, 10, 15, 20, and 25%, analyzing how the q/p varied for each dataset, see Fig. 6b. The optimal RVE size was identified by selecting the configuration with the least variation from the mean q/p while ensuring computational feasibility. Notably, datasets with 5000, 7000, and 10,000 particles showed variations within a range of −5% to 5%. The 5000-particle configuration was chosen for its computational efficiency without sacrificing accuracy.

Furthermore, pore-scale statistical distributions such as normalized pore radii ($R_i/\langle r\rangle$), throat radii ($R_{ij}/\langle r\rangle$), and pore porosity (ϕ_i) are examined, see Fig. 4. These distributions demonstrated robust statistical consistency across the particle range of 5000 to 10,000, confirming that the selected RVE size effectively captures the essential characteristics of the pore structure without incurring a high computational cost.

4. Results and discussion

4.1. Stress-strain relations and fabric evolution

The mechanical and microstructural responses of cyclically sheared granular assemblies are investigated for polydisperse granular assemblies, focusing on dense and loose states. The evolution of the stress ratio q/p and the fabric anisotropies F_c and F_p for dense and loose assemblies is shown in Fig. 7, 8 and 11. The deviatoric stress is defined as $q = \sigma_1 - \sigma_3$, and the mean confining stress as $p = (\sigma_1 + \sigma_2 + \sigma_3)/3$. The quantities F_c and F_p represent the anisotropies of the contact fabric and pore orientation, respectively.

Drained triaxial tests reveal two distinct mechanical behaviors: contracting and dilatant. A loose assembly exhibits contracting behavior, characterized by continuous volumetric contraction and deviatoric stress (q) hardening, with a lower peak of $q/p \approx 0.8$

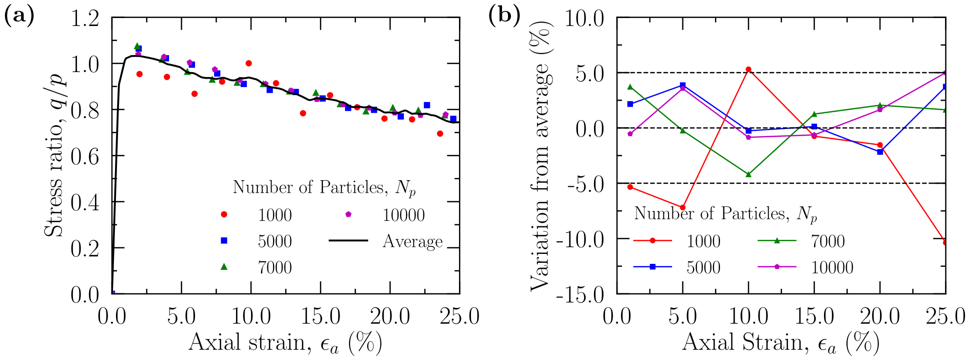

Fig. 6. (a) Comparison of the stress ratio q/p for RVEs with varying numbers of particles. The solid black line represents the average stress ratio q/p across all datasets. (b) Variation of the stress ratio q/p from the average value at different axial strain levels.

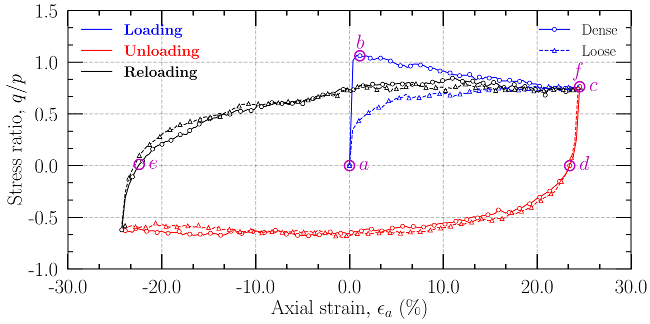

Fig. 7. Stress ratio (q/p) versus axial strain (ϵ_a) for the dense and loose granular assemblies. The dense system is represented by a solid line with circular markers, while the loose system is indicated by a dashed line with triangular markers. Loading curves are shown in blue, unloading curves in red, and reloading curves in black. Points *a*-*f* mark key deformation stages: *a* (initial, $\epsilon_a = 0\%$), *b* (peak stress), *c* (end of loading, $\epsilon_a = +25\%$), *d* and *e* (zero q/p during unloading and reloading), *f* (end of reloading, $\epsilon_a = +25\%$).

throughout shearing, stabilizing at the critical state without significant softening (Been and Jefferies, 1985). In contrast, a dense assembly displays dilatant behavior, initially undergoing slight volumetric contraction followed by dilation (associated with strain hardening), with q/p rising to a peak of 1.1 before softening to a steady-state value of 0.8 at the critical state, reflecting the dilatancy typical of dense sands (Roscoe et al., 1963; Guo and Zhao, 2013). These trends align with classical soil mechanics, where dense samples dilate and loose samples compact under shear, highlighting the significant influence of packing density on fabric evolution and mechanical response during cyclic drained shearing.

4.1.1. Contact-pore fabric coupling and directional evolution

Fig. 8a and b present the fabric anisotropy for contact fabric (F_c), computed using Eq. (5), and principal pore orientation anisotropy (F_p), derived from Minkowski moment tensors (Eq. (19)), for polydisperse loose and dense assemblies under cyclic triaxial loading, respectively. The polydisperse as well as monodisperse assemblies show a striking similarity between F_c and F_p during the loading, unloading, and reloading stages, suggesting a coupled evolution of contact and void fabrics (Fu and Dafalias, 2015). The sub-figures in Fig. 9 compare the distributions of contact normal orientations (top row) and principal pore orientations (bottom row) in the xy-plane for the polydisperse assembly at selected stages of the cyclic loading path, points *a*-*f* in Fig. 7. The contact normal distributions exhibit a pronounced directional preference that evolves systematically with the imposed deformation. In the initial isotropic state (point *a*), the distribution is nearly uniform, reflecting the RVE preparation protocol. As the dense granular assembly reaches peak strength (point *b*), strong anisotropy develops, with contact normals preferentially aligned along the compression axis. This behavior is consistent with critical state concepts, which link contact fabric anisotropy to mobilized shear resistance (Rothenburg and Bathurst, 1989). During unloading and subsequent reloading, the contact fabric progressively loses its directional bias. In particular, at points *d* and *e*, which correspond to zero stress ratio ($q/p = 0$) during unloading and reloading, respectively (see Fig. 7), the contact normal distributions approach an isotropic configuration. This indicates that the contact network responds rapidly to stress reversal and tends toward isotropy as the deviatoric stress vanishes. In contrast, the pore orientation distributions display a delayed adjustment. Although pore orientations evolve coherently with contact normals during loading, they remain noticeably anisotropic at points *d* and *e*, despite the near-isotropic contact fabric, as shown in Fig. 9j and k. Thus, at identical macroscopic stress states characterized by zero stress ratio, contact and pore fabrics do not exhibit the same degree of isotropy.

The observed anisotropy is quantified through second-order fabric tensors (see Fig. 8a and b), where the principal directions of these tensors rotate during loading-unloading-reloading cycles. During triaxial compression, the fabric tensors align their principal

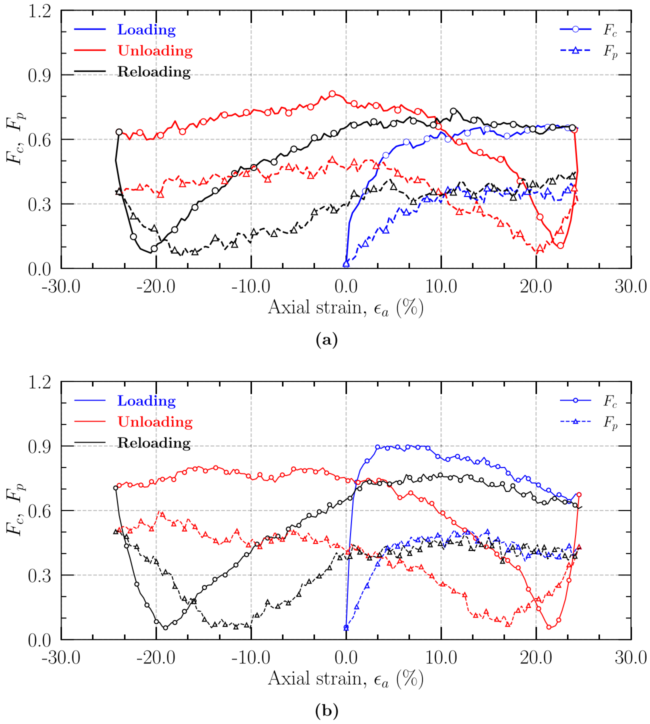

(a)

(b)

Fig. 8. Evolution of contact fabric anisotropy (F_c, solid lines) and pore orientation anisotropy (F_p, dashed lines) with axial strain for polydisperse (a) loose and (b) dense assemblies. F_c consistently exhibits a higher magnitude than F_p at corresponding strain levels, demonstrating the magnitude offset during loading (blue), unloading (red), and reloading (black) phases.

components with the global loading directions, resulting in contact normals and pore orientations predominantly concentrated vertically. This relationship reverses during unloading, with contact normals and pores reorienting horizontally. The reversibility of fabric orientation during cyclic loading offers critical insight into the micromechanical origins of the path-dependent behavior of granular materials. While Fu and Dafalias (2015) established the concept of void fabric anisotropy in 2D, and Sufian et al. (2019a) extended this to 3D monodisperse assemblies, our analysis of polydisperse and monodisperse assemblies under cyclic loading reveals two distinct features in the coupled evolution of contact and pore fabrics.

The first feature is a systematic lag in pore fabric development. Across all assemblies, the pore orientation fabric anisotropy F_p consistently trails the contact fabric anisotropy F_c, resulting in non-synchronous evolution. At a given strain level, F_p attains a lower magnitude than F_c, indicating that pore-scale anisotropy develops more gradually than contact-scale anisotropy. The second feature is a pronounced hysteresis in the contact-pore fabric phase space. When F_p is plotted directly against F_c, the loading, unloading, and reloading paths form distinct trajectories rather than collapsing onto a single curve, as shown in Fig. 10. This hysteresis is not an independent phenomenon, but a geometric manifestation of the systematic lag under cyclic loading: because F_p responds more slowly than F_c, identical contact fabric states reached at different stages of the loading cycle correspond to different pore fabric states, despite the coherent reversal of their principal orientations during cyclic loading.

The origin of hysteresis is illustrated for the polydisperse dense (PD) assembly in Fig. 10c. During initial loading from point *a* to point *c*, as the axial strain increases from $\epsilon_a = 0$ to $\epsilon_a = +25\%$, the F_c increases rapidly, reaching values of ≈ 0.9, whereas the F_p increases gradually to ≈ 0.5, reflecting the lag in pore fabric development. From point *c*, unloading is initiated by reversing the strain direction. As the axial strain decreases from $\epsilon_a = +25\%$ and passes through zero stress ratio at point *d*, the F_c and F_p decrease, but with different rates of magnitude evolution. The F_c responds more rapidly to strain reversal, while F_p decreases more slowly. Reloading then proceeds from $\epsilon_a = -25\%$ through point *e* and returns to $\epsilon_a = +25\%$ at point *f*, which coincides with point *c* in strain space. Although the fabric measures have comparable magnitudes at the end of the cycle, their intermediate evolution follows distinct paths. As a result, identical values of F_c reached during loading, unloading, or reloading correspond to different values of F_p. The hysteresis loop observed in the $F_c - F_p$ phase space, therefore, arises directly from the delayed magnitude response of pore fabric relative to contact fabric under strain reversal, even though the fabrics reverse their principal orientations coherently throughout the cyclic loading.

The lag in the two anisotropy measures reflects a hierarchical geometric emergence across different length scales. The anisotropy emerges progressively from contact-level rearrangements to particle-scale free-volume geometry and, eventually, to pore-scale structures. Contact fabric anisotropy F_c responds most directly to imposed deformation through the creation, loss, and reorientation of the geometrical contacts (Kuhn, 1999). Pore orientation anisotropy F_p, by contrast, is a collective geometric descriptor constrained by the collective arrangement of multiple particles and the surrounding free volume. Thus, anisotropy cannot emerge independently from the contact network to the pore space. To further explain the geometric origin of the lag, we introduce an intermediate fabric descriptor based on the anisotropy of particle-centered Voronoi cells. Using the same Minkowski moment tensor formalism employed for pore units, we compute the anisotropy of individual Voronoi cells and define the corresponding Voronoi fabric anisotropy F_v (Section 2.5). This ensures a consistent geometric basis for comparing fabric evolution at the contact, particle, and pore-scales. Fig. 11a and b show the evolution of F_v together with F_c and F_p for polydisperse dense and loose assemblies, respectively. For brevity, the initial loading phase ($0 \leq \epsilon_a \leq 25\%$) is shown; however, F_v is computed throughout the complete loading-unloading-reloading cycle and maintains its intermediate position between F_c and F_p across all deformation stages (see Fig. 10 for full-cycle relation). In all cases, the Voronoi fabric anisotropy evolves between the contact and pore fabric anisotropies, demonstrating that anisotropy first emerges at the particle-scale free volumes before accumulating into coherent pore-scale anisotropy.

The hierarchical ordering $F_c \rightarrow F_v \rightarrow F_p$ provides a mechanistic explanation for the observed lag between contact and pore anisotropies, emphasizing that pore-scale anisotropy does not respond instantaneously to contact statistics but emerges through progressive geometric integration. Contact rearrangements induce directional bias at the particle scale, which is integrated by the geometry of particle-centered free volumes (Voronoi cells). Once particle-scale anisotropy accumulates beyond a threshold governed by local geometric compatibility, collective reorientation and elongation of multi-particle pore units can occur. Pore fabric thus emerges as a higher-order internal variable constrained by particle-scale geometric constraints rather than an instantaneous response to contact statistics. The emergent role of particle-scale geometry in the geometrical arrangement becomes clear when the relationship between F_v and F_p is examined across all assemblies (PD, PL, MD, and ML), see Fig. 12a. A strong linear relationship is observed between F_v and F_p, indicating that pore-scale anisotropy is more constrained by particle-centered free-volume geometry than by contact fabric alone. This relationship persists across density states and particle size distributions, establishing the Voronoi fabric as the immediate geometric precursor to pore fabric evolution.

A quantitative comparison between F_c and F_p further reveals the systematic differences between monodisperse and polydisperse assemblies. Across all granular assemblies, F_c generally exceeds F_p, but the magnitude of the difference $F_c - F_p$ depends on particle size distribution. In monodisperse dense and loose assemblies, $F_c - F_p$ spans a broader range (0.0–1.0) than in polydisperse dense and loose assemblies (0.0-0.5). Linear regression analysis between F_c and F_p confirms a positive correlation, with slopes indicating a moderate to stronger coupling for monodisperse particle assemblies (MD: Pearson $r = 0.87$ and $R^2 = 0.75$; ML: Pearson $r = 0.84$ and $R^2 = 0.71$) compared to polydisperse assemblies (PD: Pearson $r = 0.70$ and $R^2 = 0.50$; PL: Pearson $r = 0.84$ and $R^2 = 0.70$). This suggests that MD assemblies exhibit more complementary fabric evolution due to increased inter-particle contacts and pore alignment under shear (Roscoe et al., 1963). In contrast, Sufian et al. (2019b) reported lower pore orientation anisotropy in 3D assemblies, potentially due to differences in pore extraction methods or shear-induced pore elongation. Additionally, Fu and Dafalias (2015) proposed a linear relationship of $F_p = 1.14F_c$ in 2D; our 3D simulations indicate that this may underestimate pore orientation anisotropy under cyclic loading, highlighting the effects of dimensionality. The greater range of $F_c - F_p$ in MD assemblies (0.0–1.0) compared to PD assemblies (0.0-0.5) reflects a higher uniformity in contact alignment, while PD assemblies display more distributed stress paths due to particle size variability (Voivret et al., 2009).

To further elucidate why the strength of $F_c - F_p$ correlation differs across MD and PD assemblies, we introduce a kinematic descriptor defined as the distance d_{vp} between a particle center and the centroid of its corresponding Voronoi cell. The scalar descriptor is a diagnostic measure of particle-free-volume kinematic compatibility, rather than a governing or constitutive parameter. A small value of d_{vp} indicates that the free volume deforms coherently with particle motion, whereas a larger value reflects increasing particle-free-volume incompatibility. Fig. 12b shows the evolution of the ensemble-averaged d_{vp} for MD and PD dense assemblies. MD assemblies exhibit systematically larger values of d_{vp} throughout deformation, indicating stronger geometric incompatibility between particle motion and free-volume reconfiguration. It is important to note that the scalar d_{vp} quantifies kinematic compatibility (local particle-free-volume) rather than the strength of fabric coupling (tensorial). In MD assemblies, the limited local accommodation of particle motion enforces collective geometric reorganization, resulting in a more coherent evolution of contact and pore fabrics. In contrast, PD assemblies exhibit enhanced local free-volume accommodation, allowing heterogeneous and spatially distributed rearrangements that weaken global fabric coherence and reduce the strength of $F_c - F_p$ correlations.

4.2. *Porosity and pore shape factor*

Fig. 13 explores the interplay between macroscale porosity and average pore shape factor $|\beta|_{avg}$ (Eq. (15)), computed from Minkowski moment tensors (Schröder-Turk et al., 2011). The dense and loose granular assemblies show a strong correlation: porosity decreases with decreasing $|\beta|_{avg}$ during contraction, peaking during dilation, and stabilizing at the steady state. The observed trends suggest that pore-shape anisotropy amplifies under shear-induced dilation (in the dense case) and diminishes during compaction (loose case), providing a mechanistic link between microstructure and bulk behavior. In Fig. 14, linear regression analyses quantify this correlation between macroscopic porosity and the ensemble-averaged $|\beta|_{avg}$, with $R^2 \geq 0.86$ across MD and PD assemblies. The adopted definition of β explicitly incorporates all three eigenvalues of the Minkowski tensor and therefore encodes the degree of anisotropy and pore shape through the relative positioning of the intermediate eigenvalue. Thus, $|\beta|_{avg}$ offers a balanced contribution from pore elongation and shape, leading to comparable slopes and similar levels of correlation with porosity across granular assemblies. This suggests that macroscopic porosity is closely associated with the combined evolution of average pore shape factor $|\beta|_{avg}$ and shape as captured by β. Differences originating from particle-size heterogeneity are therefore less pronounced in this scalar measure.

The coupling between porosity and $|\beta|_{avg}$ extends prior work by elucidating how microstructural adjustments govern bulk response. Dense assemblies' amplified $|\beta|_{avg}$ during dilation enhances pore alignment, facilitating stress redistribution, while loose assemblies' stable $|\beta|_{avg}$ reflects a more uniform compaction process. This behavior complements the observed lag in pore orienta-

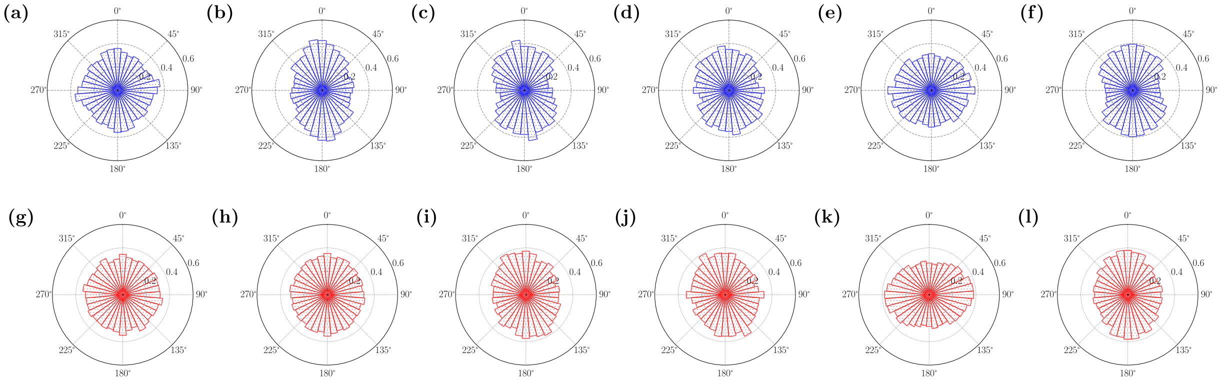

Fig. 9. Polar distributions of contact normal orientations (top row, a-f) and principal pore orientations (bottom row, g-l) in the xy-plane for polydisperse dense assembly at six deformation stages (see marked points in Fig. 7). Both distributions evolve from near-isotropic (a, g) to vertically aligned at peak strength (b, h), then redistribute horizontally during unloading (e, k), demonstrating a coordinated directional evolution.

tion anisotropy (F_p) relative to contact anisotropy (F_c) (see Fig. 10), where void spaces exhibit delayed response due to geometric constraints governing multi-particle reorganization through the hierarchical emergence $F_c \rightarrow F_v \rightarrow F_p$, and further quantified by the kinematic descriptor d_{vp}. The higher $|\beta|_{avg}$ in dense granular assemblies, coupled with their greater F_p magnitude, suggests that pore shapes serve as sensitive indicators of collective geometric reorganization, with implications for permeability evolution and shear band formation (Sufian et al., 2019b). The PD assemblies' slightly lower regression slope and R^2 values indicate distributed stress paths, reflecting an enhanced perspective on fabric heterogeneity.

4.2.1. *Particle- and pore-based metrics*

The particle and pore-scale statistical properties are interpreted as emergent consequences of the geometric constraints and the hierarchical evolution of the fabric established in the preceding sections. Fig. 15 presents the probability distribution $P(\phi_v^{-1})$, the inverse Voronoi volume fraction for polydisperse granular assemblies subjected to cyclical shear deformation. The $P(\phi_v^{-1})$ is defined as the ratio of the volume of the Voronoi cell to the enclosed particle (Guo and Zhao, 2014). These distributions are analyzed at multiple axial strain levels ($\epsilon_a = 0\%, 10\%, \text{ and } 25\%$) to capture the evolution of local packing structure during deformation. Fig. 15a, depicts the initially dense assembly, where a pronounced rightward shift of peak positions occurs with increasing strain, from approximately $\phi_v^{-1} \approx 1.65$ at the initial state to $\phi_v^{-1} \approx 1.8$ at 25% strain. This shift quantifies the shear dilatancy, a characteristic of dense granular materials that requires them to expand volumetrically to accommodate shear-induced particle reorganization. Contrasting behavior is observed in Fig. 15b for the initially loose granular assemblies. The distribution maintains relatively consistent peak positions around $\phi_v^{-1} \approx 1.7$ across all strain levels. This consistency suggests that loose assemblies undergo minimal bulk volume change despite significant particle rearrangements during shear. The insets in both figures reveal a remarkable feature: when normalized appropriately to yield dimensionless variables $\hat{\phi_v^{-1}} = \phi_v^{-1}/\langle\phi_v^{-1}\rangle$, the distributions from different strain states collapse onto a single curve well-approximated by a gamma distribution. These results indicate that while the mean values change with deformation, the normalized distributions maintain a statistically consistent form during shearing.

Figs. 16 and 17 illustrate the complementary perspective of void space evolution through pore porosity distributions $P(\phi_p)$ and pore shape anisotropy $P(\beta)$, respectively. Fig. 16a, labeled "Shear dilation" corresponds to the initially dense assembly and shows a clear rightward shift in the distribution peaks from $\phi_p \approx 0.30$ to $\phi_p \approx 0.35$ as strain increases, reflecting heterogeneous pore size changes driven by deformation mechanisms. The observed widening and skewness suggest that pore structures become increasingly varied as the dense assembly rearranges under shear. This behavior aligns with shear dilation, where larger pores emerge due to particle sliding and rotation. The shift in the peak porosity directly corresponds to a net increase in average void space, consistent with the shear-induced dilatancy observed in triaxial compression tests. Conversely, Fig. 16b, labeled "Contraction", represents the initially loose assembly and exhibits more subtle changes in distribution shape and position, consistent with the contractive tendency of loose granular materials under shear.

The probability distribution of the pore shape anisotropy $P(\beta)$, for the polydisperse dense and loose granular assemblies, exhibits a consistent trend, as shown in Fig. 17. The presence of a non-zero probability density at $\beta = 0$ suggests that the granular assembly includes shape-isotropic pore geometries, where the eigenvalues of the Minkowski tensor are equal. The persistence of these isotropic pore shapes across both isotropic and anisotropic stress states, as well as across granular assemblies, demonstrates that local geometric isotropy of the pore space can coexist with an anisotropic granular fabric. This observation highlights the ability of β to capture pore shape anisotropy in a physically meaningful manner, revealing subtle geometric features of the void structure that are not apparent from the stress state alone. Furthermore, to compare pore-scale fluctuations across deformation stages and packing states, pore-scale quantities are normalized by their ensemble-averaged values. The normalized pore-scale porosity and pore shape anisotropy are

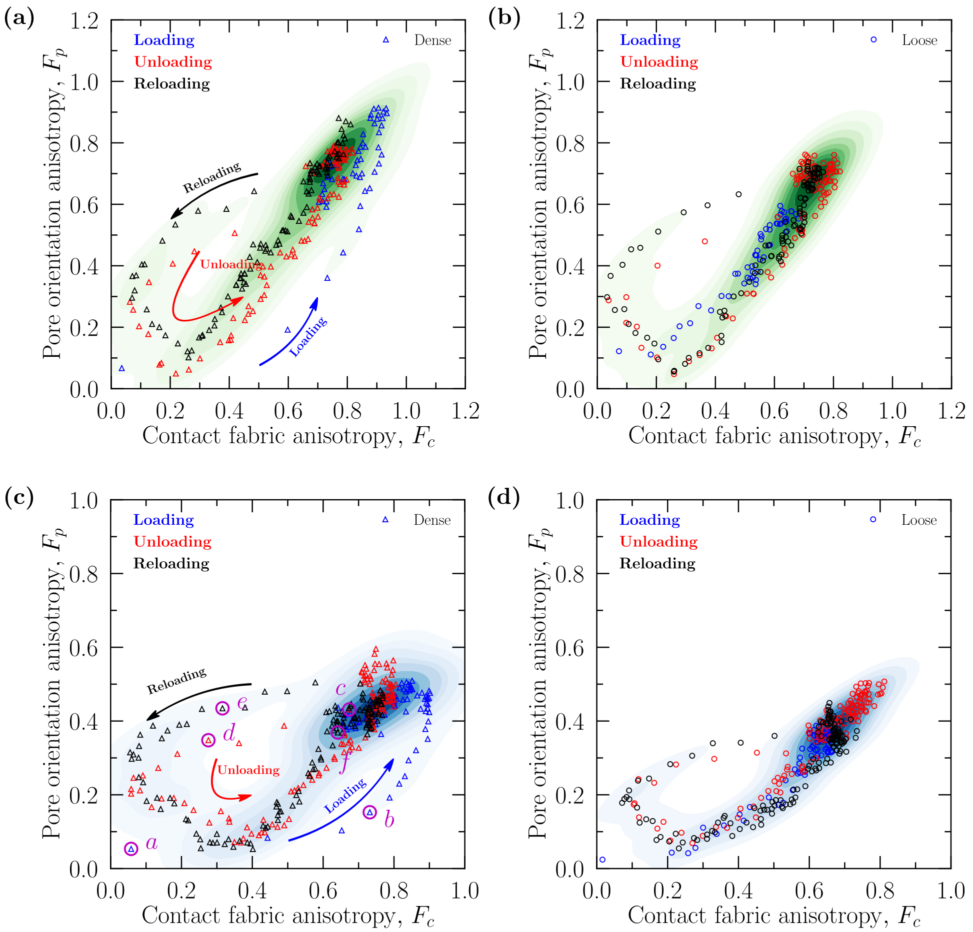

Fig. 10. Correlation between contact fabric anisotropy (F_c) and pore orientation anisotropy (F_p) for different granular assemblies during shearing. The data points represent the anisotropies during loading, unloading, and reloading stages. (a) MD, (b) ML, (c) PD and (d) PL.

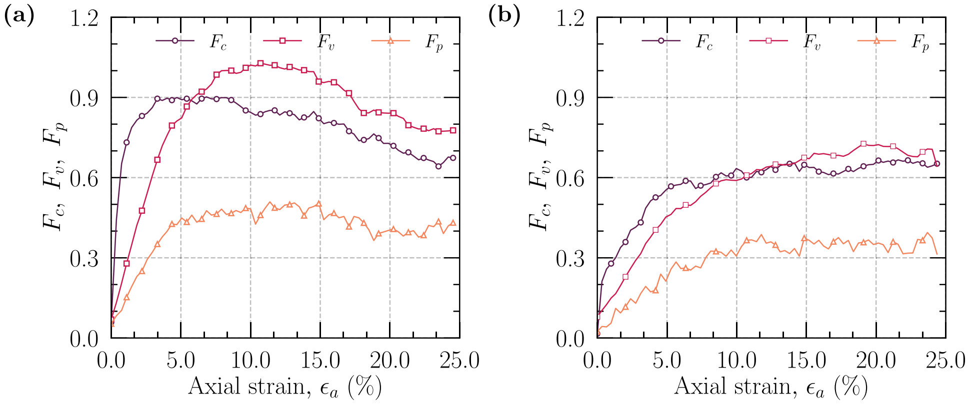

Fig. 11. Evolution of contact fabric anisotropy (F_c), Voronoi fabric anisotropy (F_v), and pore orientation anisotropy (F_p) with axial strain during the initial loading phase ($0 \le \epsilon_a \le 25$) for polydisperse (a) dense and (b) loose assemblies. Only the loading phase is shown for clarity to highlight the hierarchical ordering; F_v is computed throughout the complete cycle and used in the correlation analysis, Fig. 12. F_v evolves intermediate between F_c and F_p, demonstrating hierarchical geometric emergence $F_c \rightarrow F_v \rightarrow F_p$.

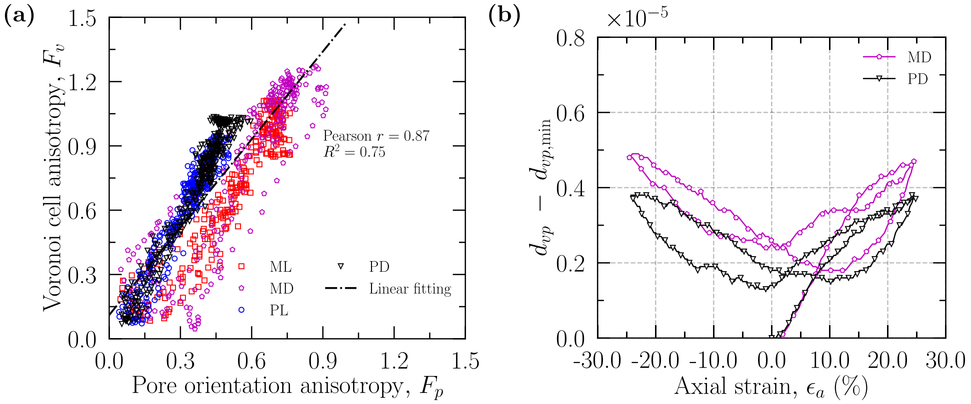

Fig. 12. (a) Linear relation between F_v and F_p across all assemblies, linear regression yields Pearson $r = 0.87$, $R^2 = 0.75$. (b) Evolution of ensemble-averaged shifted kinematic descriptor d_{vp}-$d_{vp,\min}$ with axial strain for MD and PD assemblies, where $d_{vp,\min}$ represents the minimum value. MD assemblies exhibit larger d_{vp}, indicating their greater magnitude offsets.

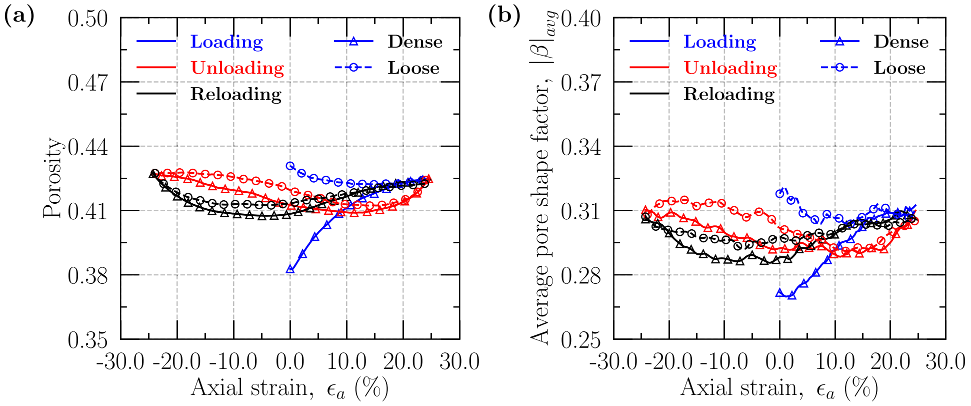

Fig. 13. Evolution of the macroscale porosity and average pore shape factor $|\beta|_{avg}$ for a cyclical sheared polydispersed granular assembly.

defined as

$$\hat{\phi}_p = \frac{\phi_p}{\langle \phi_p \rangle}, \qquad \text{and} \qquad \hat{\beta} = \frac{\beta - \beta_{min}}{\langle \beta \rangle - \beta_{min}}. \tag{24}$$

The insets in Figs. 16 and 17 reveal that the normalized distributions of pore porosity ($\hat{\phi}_p$) and shape anisotropy ($\hat{\beta}$) adhere to a gamma distribution, independent of strain level. This adherence to the gamma statistical framework corroborates theoretical predictions for disordered granular systems, where local volume and shape fluctuations are well described by k-gamma distributions (Aste and Di Matteo, 2008; Guo and Zhao, 2014; Zhao et al., 2020).

The statistical analysis of microstructures, conducted through particle-based and void-based metrics, consistently reveals a gamma distribution framework, providing insights into the evolution of disorder under shear loading. As shown in Fig. 18a-c, the probability distributions of inverse Voronoi cell fractions (ϕ_v^{-1}), pore-scale porosity (ϕ_p), and pore shape anisotropy (β) adhere to gamma distributions across both monodisperse and polydisperse assemblies, encompassing dense and loose system at different shear levels. Notably, Fig. 18a demonstrates that the scaled and shifted inverse Voronoi cell fractions exhibit nearly identical distributions at different shear levels, suggesting that the compactivity of each assembly remains statistically consistent during deformation.

Further, we fitted a k-gamma distribution to the data, determining a shape parameter k of 4.5. This value aligns with the findings of Guo and Zhao (2014), who demonstrated that local volume fluctuations in granular systems conform to a k-gamma distribution, with k typically ranging between 5 and 7 under external loading, as calculated using Eq. (25), where $(\phi_v^{-1})_{\min}$ and $\sigma_{\phi_v^{-1}}$ denotes the minimum and standard deviation, respectively. This persistence underscores the significance of the k-gamma framework in capturing the statistical properties of granular systems, encompassing both spherical and non-spherical particles (Zhao et al., 2020). The parameter k serves as a key indicator of microstructural organization (Aste and Di Matteo, 2008; Guo and Zhao, 2014).

$$k = \frac{[\langle \phi_v^{-1} \rangle - (\phi_v^{-1})_{min}]^2}{\sigma^2_{\phi_v^{-1}}}. \tag{25}$$

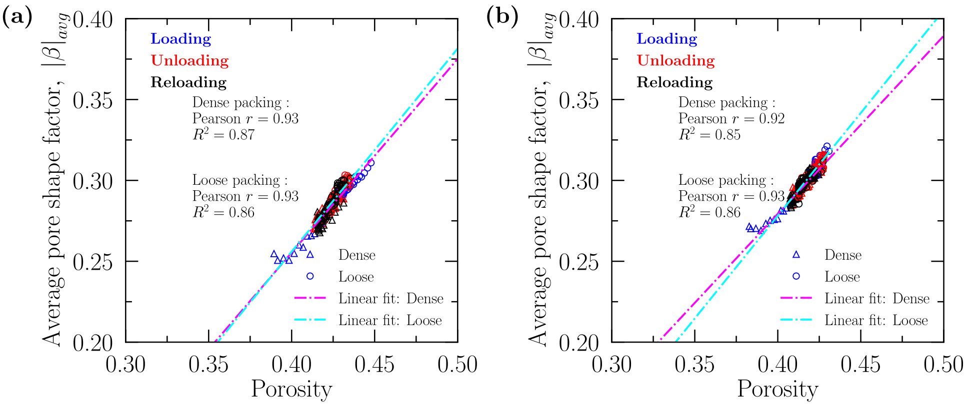

Fig. 14. Correlation between porosity and average pore shape factor $|\beta|_{avg}$ for different assemblies during shearing. A linear regression fit is illustrated, with a Pearson correlation coefficient r and R^2, indicating a correlation between the two variables. (a) Monodisperse particle assemblies and (b) Polydisperse particle assemblies.

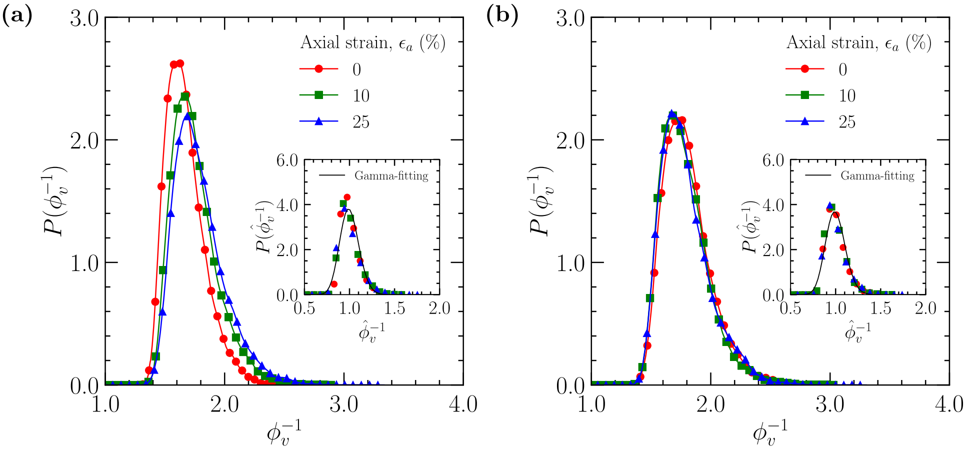

Fig. 15. The probability distribution $P(\phi_v^{-1})$ of the inverse Voronoi volume fraction for polydisperse granular assemblies subjected to cyclic shear deformation. The inset displays the normalized values $\hat{\phi_v^{-1}}$, defined as $\hat{\phi_v^{-1}} = \phi_v^{-1}/\langle\phi_v^{-1}\rangle$, (a) PD and (b) PL.

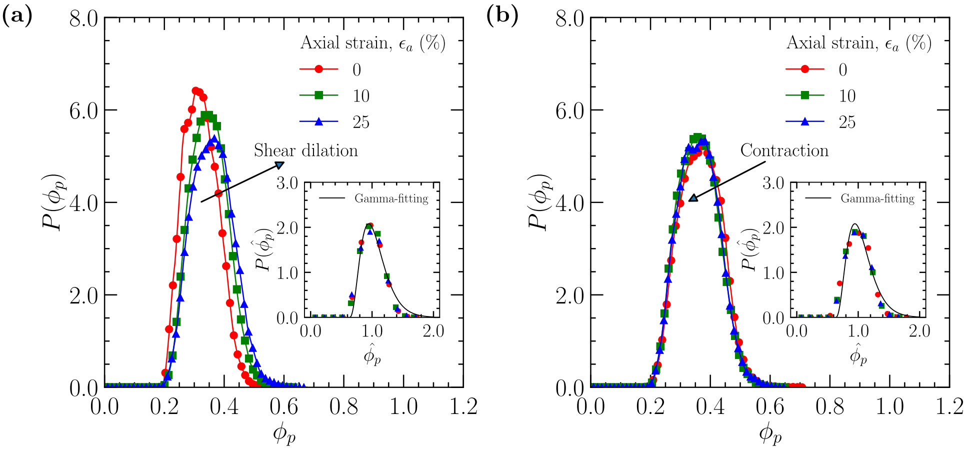

Fig. 16. The probability distribution $P(\phi_p)$ represents the pore porosity for polydisperse granular assemblies subjected to cyclic shear deformation. The inset shows the normalized values $\hat{\phi}_p$, defined as $\hat{\phi}_p = \phi_p \, / \langle\phi_p\rangle$, (a) PD and (b) PL.

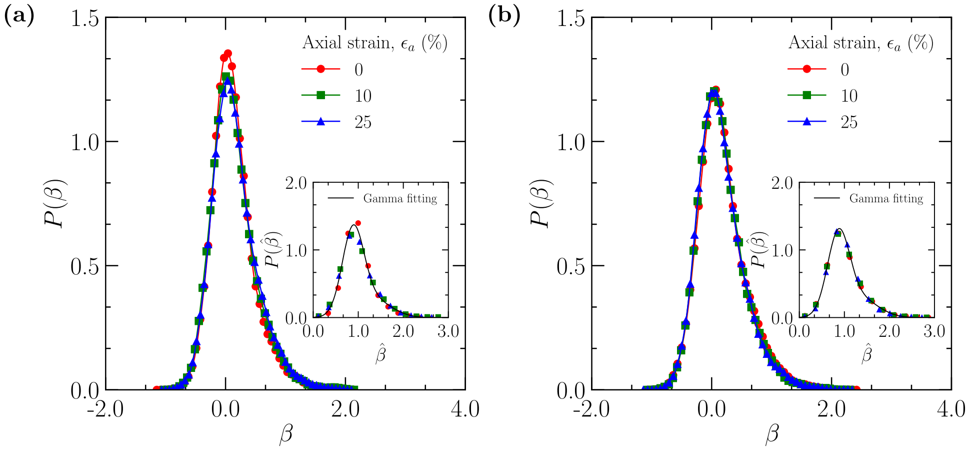

Fig. 17. The probability distribution $P(\beta)$ represents the shape factor for voids in granular assemblies. The inset shows the normalized values $\hat{\beta}$, where $\hat{\beta} = \beta - \beta_{\min}/\langle\beta\rangle - \beta_{\min}$, (a) PD and (b) PL.

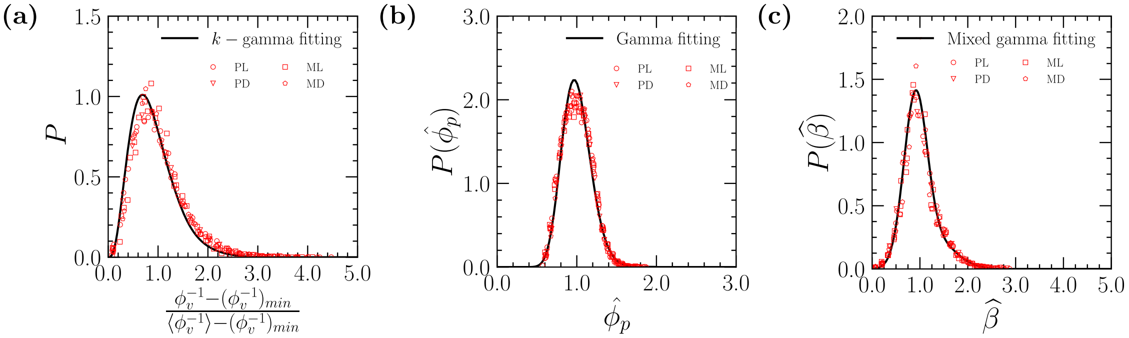

Fig. 18. Probability distributions for (a) scaled and shifted Voronoi cell fractions, (b) pore-scale porosity, and (c) pore shape anisotropy for monodisperse and polydisperse granular assemblies at different axial strains. The scaled and shifted Voronoi cell fractions are fitted with a k-gamma distribution, where the shape parameter k equals 4.5. The distributions for porosity and shape anisotropy are fitted to a gamma fit.

Similarly, the void-based metrics in Fig. 18b-c, representing the normalized $\hat{\phi}_p$ and $\hat{\beta}$, conform to a gamma distribution across all strain levels, demonstrating a robust statistical form despite deformation. This conformity holds for monodisperse and polydisperse granular assemblies, with no significant differences in the shape of the normalized distributions, reflecting the underlying consistency of the pore structure's statistical behavior under shear. The preservation of gamma statistics across both particle-based and void-based metrics highlights the consistent mechanisms governing volume and shape distributions in granular systems (Aste and Di Matteo, 2008). The persistence, reinforced by the complementary nature of these analyses, establishes the gamma distribution framework as a statistically robust tool for characterizing microstructural evolution under complex loading paths.

5. Summary and conclusions

This study established a pore-based fabric tensor framework, leveraging Minkowski moment tensors, to quantitatively characterize the anisotropic evolution of voids in granular materials under cyclic triaxial loading. Through DEM simulations of monodisperse and polydisperse granular assemblies in both dense and loose states, we decoupled the dynamic interplay between contact and void fabric, linking these microstructural metrics to macroscopic response. The principal findings are summarized as follows:

- **Non-synchronous evolution and hierarchical fabric coupling**: The evolution of pore fabric is non-synchronous with that of contact fabric. While contact anisotropy responds rapidly and reversibly to changes in loading direction, pore fabric exhibits a systematic lag, accompanied by pronounced path dependence. Identical macroscopic stress states and contact fabric configurations attained during different stages of the loading cycle correspond to distinct pore fabric states. This non-uniqueness demonstrates that pore fabric emerges as a higher order internal variable and cannot be treated as an instantaneous function of stress or contact anisotropy.

  The lag in contact-pore fabric phase space arises from geometric constraints imposed by scale separation. Contact fabric reflects grain-scale kinematics, whereas pore units are collective geometric entities spanning multiple particles. Consequently, pore fabric can only evolve through coherent reorganization of particle-scale free volume. By introducing Voronoi-cell anisotropy as a particle-scale descriptor, the analysis reveals a consistent hierarchical ordering of fabric evolution, with anisotropy emerging first at the contact scale, then at the Voronoi scale, and finally at the pore scale. This hierarchy provides a mechanistic explanation for the delayed and hysteretic evolution of pore fabric under cyclic loading.

The differences between monodisperse and polydisperse assemblies further highlight the role of particle-scale geometric compatibility. A scalar kinematic descriptor based on the offset between particle centers and Voronoi centroids serves as a diagnostic measure of particle-free-volume incompatibility, indicating that enhanced local accommodation in polydisperse systems weakens global fabric coherence, whereas monodisperse assemblies promote more collective geometric reorganization.

- **Multiscale descriptor of density and statistical organization**: Beyond orientational fabric, the hierarchical emergence of pore structure is also reflected in the collective evolution of pore geometry and its statistical organization. At the macroscopic level, the average pore shape factor, $|\beta|_{avg}$, computed directly from Minkowski tensors, exhibits a strong correlation with porosity across loading paths, consistently tracking volumetric contraction and dilation. The adopted definition of β incorporates all three eigenvalues of the Minkowski tensor, and encodes the anisotropy magnitude and pore shape through the relative positioning of the intermediate eigenvalue. In this sense, $|\beta|_{avg}$ provides a mechanics-informed geometric descriptor linking collective pore deformation to bulk density, rather than acting as an independent state variable.

  Although there is a clear path dependence in the evolution of the macroscopic pore fabric, key normalized pore-scale measures exhibit a statistically robust structure across deformation stages. Distributions of inverse Voronoi cell fractions, pore-scale porosity, and pore shape anisotropy are consistently well described by gamma-type distributions when appropriately normalized. Notably, shear-induced dilation primarily manifests as a shift in the mean pore-scale porosity, while the functional form of the normalized distributions remains largely unchanged. This coexistence of macroscopic non-uniqueness with statistically stable pore-scale geometry indicates that collective geometric constraints impose a persistent local organization, even as global fabric evolves hierarchically under cyclic loading.

This pore-based tensor framework opens several promising research avenues. In geomechanics, it can be integrated with coupled fluid-particle modeling in DEM to elucidate how pore deformation controls permeability in saturated media and fluid trapping in unsaturated media (Das, 2022; Das et al., 2025). It also provides a direct metric for analyzing the role of pore orientation and shape anisotropy in strain localization and shear band formation (Russell et al., 2016; Deng et al., 2021). Furthermore, incorporating these fabric tensors into advanced constitutive models will enhance predictions of shear strength, dilatancy, and failure (Li and Dafalias, 2012). Beyond soils, this framework is directly applicable to materials science, such as powder metallurgy, where understanding pore orientation and shape anisotropy in sintered granular compacts is critical for predicting mechanical strength and fatigue life (Saadatfar et al., 2012).

CRediT authorship contribution statement

Amiya Prakash Das: Writing – review & editing, Writing – original draft, Visualization, Software, Methodology, Investigation, Formal analysis, Data curation, Conceptualization; **Jidong Zhao:** Writing – review & editing, Supervision, Resources, Project administration, Methodology, Funding acquisition, Formal analysis, Conceptualization; **Thomas Sweijen:** Writing – review & editing, Software, Methodology, Formal analysis.

Data availability

Data will be made available on request.

Declaration of competing interest

The authors declare that they have no known competing financial interests or personal relationships that could have appeared to influence the work reported in this paper.

Acknowledgements

JZ acknowledges the financial support from National Natural Science Foundation of China (by Project No. 52439001), Research Grants Council of Hong Kong (by GRF Projects Nos. 16208224 and 16203123, CRF Project No. C7085-24G, and TRS Projects Nos. T22-606/23-R and T22-603/24N) and State Key Laboratory of Climate Resilience for Coastal Cities (SKLCRCC) (Project ITC-SKLCRCC26EG01).

Reference

Arthur, J., Menzies, B., 1972. Inherent anisotropy in a sand. Geotechnique 22 (1), 115–128.

Aste, T., Di Matteo, T., 2008. Emergence of gamma distributions in granular materials and packing models. Phys. Rev. E-Stat., Nonlinear, Soft Matter Phys. 77 (2), 021309.

Been, K., Jefferies, M.G., 1985. A state parameter for sands. Géotechnique 35 (2), 99–112.

Blatny, L., Löwe, H., Gaume, J., 2023. Microstructural controls on the plastic consolidation of porous brittle solids. Acta Mater. 250, 118861.

Catalano, E., Chareyre, B., Barthélemy, E., 2014. Pore-scale modeling of fluid-particles interaction and emerging poromechanical effects. Int. J. Numer. Anal. Methods Geomech. 38 (1), 51–71.

Chan, H.T., Kenney, T.C., 1973. Laboratory investigation of permeability ratio of new liskeard varved soil. Canad. Geotech. J. 10 (3), 453–472.

Chueire, J., Daouadji, A., Nicot, F., Wautier, A., 2023. On the extension of the grain loop concept from 2d to 3d granular assemblies. Granular Matter 25 (3), 57.

Cresswell, A., Powrie, W., 2004. Triaxial tests on an unbonded locked sand. Géotechnique 54 (2), 107–115.

Das, A.P., 2022. Micromechanical Modelling of Triphasic Granular System. Ph.D. thesis. Hong Kong University of Science and Technology (Hong Kong).

Das, A.P., Zhao, J., Sweijen, T., 2025. Micromechanical modeling of triphasic granular media. Proceedings of the National Academy of Sciences 122 (18), e2420314122.

Deng, N., Wautier, A., Thiery, Y., Yin, Z.-Y., Hicher, P.-Y., Nicot, F., 2021. On the attraction power of critical state in granular materials. J. Mech. Phys. Solids 149, 104300.

Desrues, J., 2004. Tracking strain localization in geomaterials using. In: Xray CT for Geomaterials: Soils, Concrete, Rocks International Workshop on Xray CT for Geomaterials, Kumamoto, Japan. CRC Press, p. 15.

Fonseca, J., O'sullivan, C., Coop, M.R., Lee, P.D., 2012. Non-invasive characterization of particle morphology of natural sands. Soils Found. 52 (4), 712–722.

Fu, P., Dafalias, Y.F., 2015. Relationship between void-and contact normal-based fabric tensors for 2d idealized granular materials. Int. J. Solids Struct. 63, 68–81.

Gao, Z., Zhao, J., Li, X.-S., Dafalias, Y.F., 2014. A critical state sand plasticity model accounting for fabric evolution. Int. J. Numer. Anal. Methods Geomech. 38 (4), 370–390.

Ghedia, R., O'Sullivan, C., 2012. Quantifying void fabric using a scan-line approach. Comput. Geotech. 41, 1–12.

Guo, N., Zhao, J., 2013. The signature of shear-induced anisotropy in granular media. Comput. Geotech. 47, 1–15.

Guo, N., Zhao, J., 2014. Local fluctuations and spatial correlations in granular flows under constant-volume quasistatic shear. Phys. Rev. E 89 (4), 042208.

Inglis, D., Pietruszczak, S., 2003. Characterization of anisotropy in porous media by means of linear intercept measurements. Int. J. Solids Struct. 40 (5), 1243–1264.

Jiang, X., Matsushima, T., Blumenfeld, R., 2025. Coordinated stress-structure self-organization in granular packing. Phys. Rev. E 111 (4), 045406.

Joekar-Niasar, V., Hassanizadeh, S.M., Dahle, H.K., 2010. Non-equilibrium effects in capillarity and interfacial area in two-phase flow: dynamic pore-network modelling. J. Fluid Mech. 655, 38–71.

Johnson, K.L., Johnson, K.L., 1987. Contact mechanics. Cambridge university press.

Kawamoto, R., Andò, E., Viggiani, G., Andrade, J.E., 2018. All you need is shape: predicting shear banding in sand with LS-DEM. J. Mech. Phys. Solids 111, 375–392.

Ken-Ichi, K., 1984. Distribution of directional data and fabric tensors. Int. J. Eng. Sci. 22 (2), 149–164.

Konishi, J., Naruse, F., 1988. A note on fabric in terms of voids. In: Studies in Applied Mechanics. Elsevier. Vol. 20, pp. 39–46.

Kuhn, M.R., 1999. Structured deformation in granular materials. Mech. Mater. 31 (6), 407–429.

Kuhn, M.R., Sun, W., Wang, Q., 2015. Stress-induced anisotropy in granular materials: fabric, stiffness, and permeability. Acta Geotech. 10, 399–419.

Kuwano, R., Jardine, R.J., 2002. On the applicability of cross-anisotropic elasticity to granular materials at very small strains. Géotechnique 52 (10), 727–749.

Li, W., Juanes, R., 2024. Dynamic imaging of force chains in 3d granular media. Proceedings of the National Academy of Sciences 121 (14), e2319160121.

Li, X., Li, X.-S., 2009. Micro-macro quantification of the internal structure of granular materials. J. Eng. Mech. 135 (7), 641–656.

Li, X.S., Dafalias, Y.F., 2012. Anisotropic critical state theory: role of fabric. J. Eng. Mech. 138 (3), 263–275.

Ma, Z., Jia, M., Liu, J., Xu, W., 2024. Microstructural characterization of DEM-based random packings of monodisperse and polydisperse non-convex particles. J. Chem. Phys. 161 (18).

Majmudar, T.S., Behringer, R.P., 2005. Contact force measurements and stress-induced anisotropy in granular materials. Nature 435 (7045), 1079–1082.

Mei, J., Ma, G., Liu, J., Nicot, F., Zhou, W., 2023. Modeling shear-induced solid-liquid transition of granular materials using persistent homology. J. Mech. Phys. Solids 176, 105307.

Oda, M., 1982. Fabric tensor for discontinuous geological materials. Soils Found. 22 (4), 96–108.

Oda, M., Nemat-Nasser, S., Konishi, J., 1985. Stress-induced anisotropy in granular masses. Soils Found. 25 (3), 85–97.

Ouadfel, H., Rothenburg, L., 2001. Stress–force–fabric'relationship for assemblies of ellipsoids. Mech. Mater. 33 (4), 201–221.

Roscoe, K.H., Schofield, A.N., Thurairajah, A., 1963. Yielding of clays in states wetter than critical. Geotechnique 13 (3), 211–240.

Rothenburg, L., Bathurst, R.J., 1989. Analytical study of induced anisotropy in idealized granular materials. Geotechnique 39 (4), 601–614.

Russell, S., Walker, D.M., Tordesillas, A., 2016. A characterization of the coupled evolution of grain fabric and pore space using complex networks: pore connectivity and optimized flows in the presence of shear bands. J. Mech. Phys. Solids 88, 227–251.

Saadatfar, M., Mukherjee, M., Madadi, M., Schröder-Turk, G.E., Garcia-Moreno, F., Schaller, F.M., Hutzler, S., Sheppard, A.P., Banhart, J., Ramamurty, U., 2012. Structure and deformation correlation of closed-cell aluminium foam subject to uniaxial compression. Acta Mater. 60 (8), 3604–3615.

Satake, M., 1992. A discrete-mechanical approach to granular materials. Int. J. Eng. Sci. 30 (10), 1525–1533.

Schröder-Turk, G.E., Mickel, W., Kapfer, S.C., Klatt, M.A., Schaller, F.M., Hoffmann, M. J.F., Kleppmann, N., Armstrong, P., Inayat, A., Hug, D., et al., 2011. Minkowski tensor shape analysis of cellular, granular and porous structures. Adv. Mater. 23 (22–23), 2535–2553.

Schröder-Turk, G.E., Mickel, W., Kapfer, S.C., Schaller, F.M., Breidenbach, B., Hug, D., Mecke, K., 2013. Minkowski tensors of anisotropic spatial structure. New J. Phys. 15 (8), 083028.

Schröder-Turk, G.E., Mickel, W., Schröter, M., Delaney, G.W., Saadatfar, M., Senden, T.J., Mecke, K., Aste, T., 2010. Disordered spherical bead packs are anisotropic. Europhys. Lett. 90 (3), 34001.

Sitharam, T.G., Vinod, J.S., Ravishankar, B.V., 2009. Post-liquefaction undrained monotonic behaviour of sands: experiments and DEM simulations. Géotechnique 59 (9), 739–749.

Šmilauer, V., Catalano, E., Chareyre, B., Dorofeenko, S., Duriez, J., Gladky, A., Kozicki, J., Modenese, C., Scholtès, L., Sibille, L., et al., 2010. Yade reference documentation. Yade Documentation 474 (1).

Sufian, A., Knight, C., O'Sullivan, C., van Wachem, B., Dini, D., 2019a. Ability of a pore network model to predict fluid flow and drag in saturated granular materials. Comput. Geotech. 110, 344–366.

Sufian, A., Russell, A.R., Whittle, A.J., 2019b. Evolving pore orientation, shape and size in sheared granular assemblies. Granular Matter 21 (1), 1–13.

Sufian, A., Russell, A.R., Whittle, A.J., Saadatfar, M., 2015. Pore shapes, volume distribution and orientations in monodisperse granular assemblies. Granular Matter 17 (6), 727–742.

Sweijen, T., Hassanizadeh, S.M., Chareyre, B., Zhuang, L., 2018. Dynamic pore-scale model of drainage in granular porous media: the pore-unit assembly method. Water Resour. Res. 54 (6), 4193–4213.

Thornton, C., Cummins, S.J., Cleary, P.W., 2011. An investigation of the comparative behaviour of alternative contact force models during elastic collisions. Powder Technol. 210 (3), 189–197.

Ventouras, K., Coop, M.R., 2009. On the behaviour of thanet sand: an example of an uncemented natural sand. Géotechnique 59 (9), 727–738.

Vlahinić, I., Andò, E., Viggiani, G., Andrade, J.E., 2014. Towards a more accurate characterization of granular media: extracting quantitative descriptors from tomographic images. Granular Matter 16 (1), 9–21.

Voivret, C., Radjai, F., Delenne, J.-Y., El Youssoufi, M.S., 2009. Multiscale force networks in highly polydisperse granular media. Phys. Rev. Lett. 102 (17), 178001.

Wan, R.G., Guo, P.J., 2004. Stress dilatancy and fabric dependencies on sand behavior. J. Eng. Mech. 130 (6), 635–645.

Wang, Y.H., Mok, C.M., 2008. Mechanisms of small-strain shear-modulus anisotropy in soils. J. Geotech. Geoenviron. Eng. 134 (10), 1516–1530.

Xing, Y., Yuan, Y., Yuan, H., Zhang, S., Zeng, Z., Zheng, X., Xia, C., Wang, Y., 2024. Origin of the critical state in sheared granular materials. Nat. Phys. 20 (4), 646–652.

Yuan, C., Chareyre, B., 2017. A pore-scale method for hydromechanical coupling in deformable granular media. Comput. Methods Appl. Mech. Eng. 318, 1066–1079.

Zhao, S., Zhao, J., Guo, N., 2020. Universality of internal structure characteristics in granular media under shear. Phys. Rev. E 101 (1), 012906.